Sensitivity Studies of Four-Dimensional Local Ensemble Transform Kalman Filter Coupled With WRF-Chem Version 3.9.1 for Improving Particulate Matter Simulation Accuracy

Jianyu Lin[1,2], Tie Dai[2*], Lifang Sheng[1], Weihang Zhang[1],

Shangfei Hai[3], Yawen Kong[4]

[1] College of Oceanic and Atmospheric Sciences, Ocean University of China, Qingdao,

266100, China

[2] State Key Laboratory of Numerical Modeling for Atmospheric Sciences and Geophysical

Fluid Dynamics, Institute of Atmospheric Physics, Chinese Academy of Sciences, Beijing,

China

[3] CMA Earth System Modeling and Prediction Centre, China Meteorological Administration

(CMA), Beijing 100081

[4] State Key Laboratory of Remote Sensing Science, Aerospace Information Research

Institute, Chinese Academy of Sciences, Beijing 100101, China

Correspondence:Tie Dai (daitie@mail.iap.ac.cn)

Abstract: Accurately simulate severe haze events through numerical models remains challenging because of uncertainty in anthropogenic emissions and physical parameterizations of particulate matter ($PM_{2.5}$ and PM_{10}). In this study, a coupled WRF-Chem/four-dimension local ensemble transform Kalman filter (4D-LETKF) data assimilation system has been successfully developed to optimize particulate matter concentration by assimilating hourly

ground-based observations in winter over the Beijing-Tianjin-Hebei region and surrounding

provinces. The effectiveness of 4D-LETKF system and its sensitivity to ensemble member size

and length of assimilation window have been investigated. The promising results show that

significant improvements have been made by analysis in the simulation of particulate matter

during severe haze event. The assimilation reduces root mean square errors of $PM_{2.5}$ from 69.93

to 31.19 $\mu g\ m^{-3}$ and of PM_{10} from 106.88 to 76.83$\mu g\ m^{-3}$. Smaller RMSEs and larger correlation

coefficients in the analysis of $PM_{2.5}$ and PM_{10} are observed across nearly all verification stations,

indicating that the 4D-LETKF assimilation optimizes the simulation of $PM_{2.5}$ and PM_{10}

concentration efficiently. Sensitivity experiments reveal that the combination of 48 hours of

assimilation window length and 40 ensemble members shows best performance for reproducing

severe haze event. In view of the performance of ensemble members, increasing ensemble

member size improves ensemble spread among each forecasting member, facilitates the spread

of state vectors about $PM_{2.5}$ and PM_{10} information in the first guess, favors the variances

between each initial condition in the next assimilation cycle and leads to better simulation

performance both in severe and moderate haze events. This study advances our understanding

about the selection of basic parameters in the 4D-LETKF assimilation system and the

performance of ensemble simulation in a particulate matter polluted environment.

Key words: 4D-LETKF, severe haze simulation, ensemble member size, length of assimilation

window

1. Introduction

Although great progress about air pollution control has been made during recent years,

45 China is facing the highest levels of particulate matter in the world (van Donkelaar et al., 2016).

46 Particulate matter consists of $PM_{2.5}$ and PM_{10}, refers to particles with aerodynamic diameters

47 of less than 2.5 and 10 μm, respectively. High concentration of particulate matter is a major

48 factor for severe haze events (air quality index larger than 200) in the Beijing-Tianjin-Hebei

49 (BTH) region of China, especially during winter (Yan et al., 2016, Zhang et al., 2018).

50 Numerical models are considered to be useful tools for simulating haze events as for taking

51 complex physical and chemical mechanisms into account, but the uncertainty in emissions and

52 physical parameterizations still remain a significant barrier in improving the simulation

53 accuracy (Gao et al., 2017, Feng et al., 2018).

54   As an effective statistical approach, data assimilation is capable of improving the accuracy

55 of pollution simulations by limiting the performance of models. Lots of data assimilation

56 approaches have been applied to the atmospheric science, including three-dimension variation

57 (3D-Var) (Lorenc 1986; Parrish and Derber 1992; Sun et al., 2020), four-dimension variation

58 (4D-Var) (Huang et al. 2009; Benedetti et al., 2009), ensemble Kalman filter algorithms and

59 their variants (Evensen 1994; Whitaker and Hamill 2002; Miyazaki et al., 2012a), etc. Among

60 them, four-dimension local ensemble transform Kalman filter (4D-LETKF) has shown unique

61 characteristics in numerical simulation (Evensen, 2003, Kong et al., 2021). Firstly, derived from

62 finite forecasting members, the background error covariance matrix of 4D-LETKF features

63 flow-dependent characteristics, and the linear combinations of ensemble members produce

64 global analysis (Hunt et al., 2007). Secondly, the computational time for 4D-LETKF remains

65 robust as the observation numbers increase, exhibiting strong computational ability in the

66 parallel architecture when assimilate various measurements (Miyoshi et al., 2007; Hunt et al.,

67 2007, Dai et al., 2021). Lastly, 4D-LETKF can assimilate time slots of asynchronous

68 observations to optimize the current state within the assimilation window, which efficiently

69 improves the quality of pollution prediction (Evensen, 2003, Ott et al., 2004, Dai et al., 2019,

70 Cheng et al., 2019).

71   The characteristics of 4D-LETKF underscore the importance of ensemble member size

72 and length of assimilation window on its effectiveness. The ensemble member decides the

73 background error covariance matrix, representing the uncertainty in ensemble simulations

74 (Peng et al., 2017). 4D-LETKF considers approximate model trajectories by linear

75 combinations of the background ensemble trajectories. However, limited numbers of ensemble

76 members may bring about insufficient dispersion of ensemble systems (Hunt et al., 2004). In

77 addition, 4D-LETKF system can greatly improves the utilization rate of observations by

78 constrain the state variables in asynchronous hourly slot within the assimilation window. A

79 longer assimilation window efficiently reduces computational load by avoiding frequent

80 switches between state and forecast variables. But the trajectories over a long length of

81 assimilation window may diverge enough that linear combinations will not approximate the

82 model trajectories. Moreover, the model ensemble trajectory may not fit the observations well

83 over the entire interval with the presence of model errors (Dai et al., 2019). Many studies have

84 discussed the choice of these two parameters for ensemble Kalman filter algorithms and their

85 variants. When optimizing hourly aerosol fields by satellite observations, Cheng et al. (2019)

86 revealed that the forecast with a 24-hour assimilation window was comparable to those with 1-

87 hour, the root mean square error for AOD are 0.091 and 0.110, respectively, indicating the

88 weights determined at the end of the 24 hours assimilation window are valid to optimize the

89   ensemble trajectories. While Dai et al. (2019) proposed that over 80% of the hourly assimilation

90   efficiencies for the 1-hour assimilation window are higher than those with 6- or 24-hours in

91   4D-LETKF experiments, suggesting that assimilation efficiency decreases with the increase of

92   the assimilation window interval. These different opinions reveal that there is still a large

93   uncertainty about selection of parameters in 4D-LETKF assimilation system.

94   The accuracy simulation of severe haze events with air quality index (AQI) larger than 200

95   has been a challenging problem for a long time, posing severe threats to human daily life and

96   public health (Wang et al., 2014, Kong et al., 2021, Gao et al., 2017). Although 4D-LETKF has

97   unique advantages in computational efficiency and analysis, there are few researches

98   investigate the impacts of 4D-LETKF assimilation on pollutant simulation especially in severe

99   haze events, in addition, it is also imperative to explore the basic optimal combination of

100   assimilation parameters and its explanation in this method. Our major objectives are not only

101   to evaluate the performance of 4D-LETKF in reproducing particulate matter concentration

102   during severe haze event, but also to summarize the influence rules of ensemble size and

103   assimilation window length on particulate matter simulation, and explore whether these rules

104   are applicable to moderate haze event (air quality index smaller than 200) as well. The results

105   have great significance to verify and quantify the effect of 4D-LETKF assimilation on

106   numerical simulations of $PM_{2.5}$ and PM_{10}, subsequently providing a general rule for parameter

107   selection in the 4D-LETKF during severe haze events. Herein, we utilize 4D-LETKF system

108   which was coupled with Weather Research and Forecasting with Chemistry (WRF-Chem)

109   model to improve simulative skill of particulate matter among northern China during the winter

110   of 2020. Section 2 briefly introduces detail setting of WRF-Chem model, 4D-LETKF,

111 observations and numerical experiment designs. Section 3 compares the assimilation with those

112 in the prior simulation, summarizes and explains sensitivity rules for parametric selection, and

113 followed by a conclusion in Section 4 lastly.

114 2. Methodology

115 2.1 Configuration of the forecast model

116 In our implementation, the fully coupled "online" WRF-Chem version 3.9.1 is employed

117 as numeral forward model to describe the meteorological and chemical conditions

118 simultaneously, which fully considers extensive chemical transport processes including

119 advection, convection and sedimentation processes (Grell et al., 2005). The WRF-Chem model

120 is configured with two domains (d01 and d02), both using 100 (west–east) ×100 (south–north)

121 grid points, but with horizontal resolutions of 30 and 10 km, respectively. As shown in Figure

122 1(a), the d01 domain covers most part of East Asia, and the area under the blue shadow is the

123 d02 domain. The vertical grid contains 40 full sigma levels, extending from the surface to 50

124 hPa.

125 The initial and lateral boundary conditions of meteorological fields are derived from the

126 National Centers for Environmental Prediction Final (FNL) analysis data with a spatial

127 resolution of 1°×1° and temporal interval of 6 hours. A state-of-the-art and highly non-linear

128 gas-phase chemical mechanism Regional Atmospheric Chemistry Mechanism (RACM)

129 (Stockwell et al., 1997) is selected as gas phase mechanism, and Goddard Chemistry Aerosol

130 Radiation and Transport (GOCART) (Schwartz et al., 2012) is adopted as aerosol mechanism.

131 The parameterization scheme used in research is shown in Table 1.

132 Table 1. WRF-Chem parameterization scheme in this study.

Parameterization	WRF-Chem option
Microphysics	Morrison 2–moment Scheme (Morrison et al., 2019)
Longwave radiation	RRTMG Longwave Scheme (Iacono et al., 2008)
Shortwave radiation	RRTMG Shortwave Scheme (Iacono et al., 2008)
Planetary boundary layer	YSU Scheme (Hong et al., 2006)
Cumulus parameterization	Grell 3D Ensemble Scheme (Grell et al., 1993)
Land surface model	Noah (Tewari et al., 2004)

133

134   The anthropogenic emissions are obtained from the Multi-resolution Emission Inventory

135 for China compiled by Tsinghua University (MEIC, http://www.meicmodel.org/). The

136 inventory includes anthropogenic emissions from agriculture, industry, power, residential and

137 transportation sectors (Zheng et al., 2021). Inventory with a spatial resolution of $0.25° \times 0.25°$

138 and has been interpolated to match the simulation resolution. The biogenic emissions are

139 calculated online by Guenther scheme (Guenther et al. 1995). The $PM_{2.5}$, PM_{10} concentrations

140 output from WRF-Chem are linearly interpolated to site observations. The evaluation of

141 uncertainty in the emission inventory has been shown in previous research (Zhang et al., 2009).

142

143
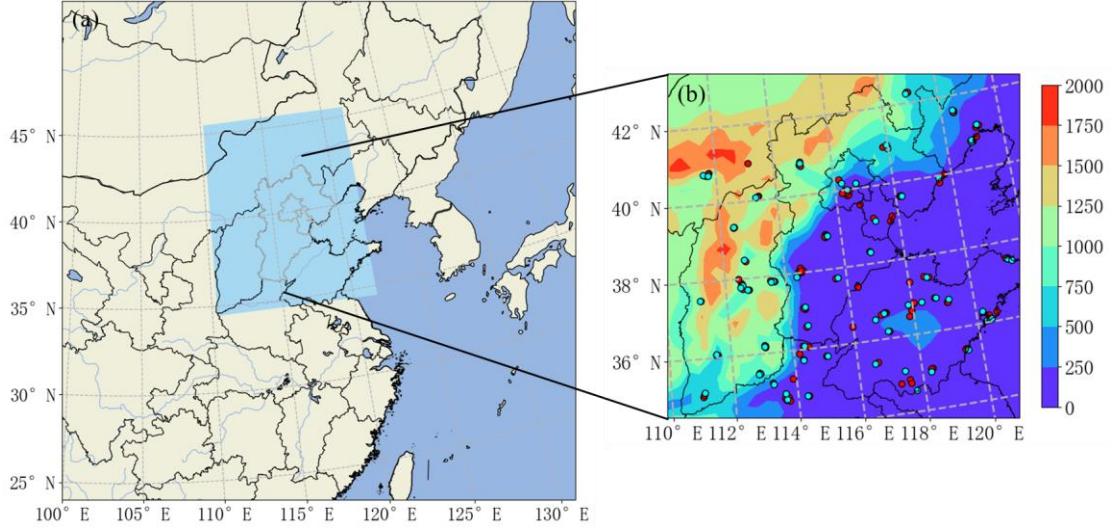
144   Figure 1. (a) WRF-Chem model domains. The grey border implies the BTH region. (b)

145   Location of assimilated and independent verification observation sites with topography (units:

146   m). The red and blue dot implies the assimilated and independent verification observation

147   site, respectively.

148   2.2 The 4D-LETKF algorithm and the state variables

149   The 4D-LETKF coupled with WRF-Chem Model is implemented to investigate the

150   influence of assimilation on particulate matter simulation in this research. In this section, we

151   introduce the 4D-LETKF algorithm and corresponding state variables briefly, more detailed

152   information can be found in Hunt et al. (2007). The LETKF features a flow-dependent

153   covariance matrix from ensemble simulation and determines the analysis ensemble mean $\overline{x^a}$

154   (a posteriori) according to the following formula:

155    $$\bar{x}^a = \bar{x}^b + X^b \bar{w}^a$$

156   where $\bar{x}^b$ and X^b denote ensemble mean of first guess and background ensemble

157   perturbations, respectively. The ensemble perturbation matrix X^b is calculated as $x^b(i) - \bar{x}^b$

158    $\{i = 1, 2, ..., k\}$, which k represents the ensemble member size. The perturbation weight matrix

159    $\bar{w}^a$ is the Kalman gain which linearly determines the increment between the analysis and the

160   first guess, and can be calculated as:

$$\overline{w}^a = \widetilde{P^a}\left(Y^b\right)^T R^{-1}(y^0 - \bar{y}^b)$$

162   where $\widetilde{P^a}$ is analysis error covariance in ensemble space. y^0 and $\bar{y}^b$ denote the

163   observations vector and ensemble mean background observations, respectively. Ensemble

164   mean background observations derived from applying observation vector to ensemble member

165   state vector H ($\bar{x}^b$). The matrix R is the observation error covariance matrix. The matrix Y^b

166   represents ensemble background observation perturbations, whose i th columns is $y^b(i) - \bar{y}^b$,

167    $\{i = 1, 2, ..., k\}$. $\widetilde{P^a}$ can be obtained as:

$$\widetilde{P^a} = [(k-1)I/\rho + (Y^b)^T R^{-1} Y^b]^{-1}$$

169   where I denotes the identity matrix and k is ensemble member size. The multiplicative inflation

170   factor ρ is necessary to avoid the filter divergence (Anderson and Anderson, 1999, Sekiyama

171   et al., 2010), so which is set to 1.1 to inflate the analysis covariance (Dai et al., 2019, Anderson,

172   2007). Analysis ensemble perturbations X^a is calculated by:

$$X_a = X^b\left[(k-1)\widetilde{P^a}\right]^{1/2} = X^b W^a$$

174   Calculated by the sum of the $\bar{x}^a$ and each of the columns of X^a, the ensemble analyses are

175   served as optimal initial conditions in each ensemble member to generate the first guess in the

176   next cycle.

177   Figure 2 is the flow chart of the WRF-Chem/4D-LETKF assimilation system applied in

178   our implementation. The system conducts these processes within each assimilation cycle. The

179   4D-LETKF generates a flow-dependent background error covariance matrix by ensemble

180   member. Given that the emissions inventory is an important source of uncertainty in simulation

181   (Pagowski and Grell, 2012), the research randomly perturbs anthropogenic emissions of PM,

black carbon (BC) and organic carbon (OC) in January for each member to create the ensemble

members, and the perturbation follows a log-normal distribution in the k-dimensional space.

The mean values of perturbations of $PM_{2.5}$, PM_{10}, BC and OC emissions are equal to 1, and the

variances of these emissions are set according to corresponding uncertainty in MEIC inventory

(130%, 132%, 208%, 258% for $PM_{2.5}$, PM_{10}, BC, OC, respectively) (Luo et al., 2023). Such

ensemble anthropogenic emissions are perfect correlation in spatial and temporal dimension

and should not be regarded as overly restrictive (Schutgens et al., 2010, Dai et al., 2021). This

study only adds one times of perturbations into emissions at the first cycle of assimilation to

provide the information spread of particulate matter. It is enough to make most of the site

information affect the first-guess field. The WRF-Chem/4D-LETKF system propagates the

ensemble forward simulation for the entire assimilation window time and outputs the first guess

fields at each hourly time slot. The ensemble mean of first guess ($\bar{x}^b$) and background ensemble

perturbations (X^b) can be obtained from ensemble member here. Combining observation and

observation operator, the innovation ($y^0 - \bar{y}^b$) and Y^b can be obtained in each time slot. The

perturbation weight matrix $\bar{w}^a$ is valid within a relative short assimilation window (e.g., 24 or

48 hours) (Hunt et al., 2004, Cheng et al., 2019). The analysis ensemble derived from $\bar{w}^a$ at

the end of time slots will serve as chemical initial conditions for the next assimilation window.

As the cycle of assimilation proceed, a linear combination of analysis ensemble is continuously

obtained.
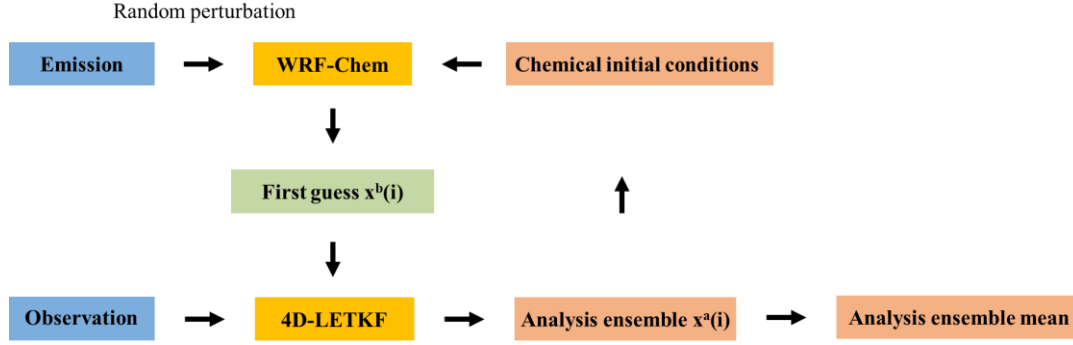
Figure 2. Flow chart of the WRF-Chem/4D-LETKF assimilation system for particulate

matter.

The ensemble Kalman filter generally encounters a spurious long-distance correlation

problem because of the limited numbers of ensemble members (Miyazaki et al., 2012a). To

avoid the problem above, it is necessary to apply observation localizations to filter observation

from a long distance. 4D-LETKF offers a flexible choice of observation localizations in

horizontal, vertical and temporal dimensions for each grid point (Cheng et al., 2019). In this

study, the horizontal localization factor is calculated as Gaussian function (Miyoshi et al., 2007),

which gradually reduces the effect of observation as the increasing departure from the analysis

grid:

$$f(r) = \exp(-r^2/2\sigma^2)$$

Here, r represents physical distance from observation to analysis grid and σ represents

localization length. We limit the localization factor from 0 to 3.65 times the localization length

(Zhao et al., 2015), ignoring the observation beyond 3.65 times the localization length to the

analysis grid.

The selection of the state variables depends on the generative mechanism of aerosol. As a

result, 16 kinds of WRF-Chem/GOCART aerosol variables are treated as state variables. For

the $PM_{2.5}$ observations, the observation operator is described as:

220
$$y_{PM_{2.5}}^b = \rho_d[P_{2.5} + 1.375S + 1.8(OC_1 + OC_2)$$

221
$$+BC_1 + BC_2 + D_1 + 0.286D_2 + S_1 + 0.942S_2]$$

222   where ρ_d present the dry-air density, $P_{2.5}$ is the fine unspecified aerosol contributions,

223   S represents sulfate, OC_1 and OC_2 are hydrophobic and hydrophilic organic carbon, respectively.

224   BC_1 and BC_2 are hydrophobic and hydrophilic black carbon, D_1 and D_2 are dusts with effective

225   radii of 0.5 and 1.4 μm, and S_1 and S_2 are sea salts with effective radii of 0.3 and 1.0 μm,

226   respectively (Peng et al., 2018).

227   Similarly, the observation operator for PM_{10} is shown as below:

228
$$y_{PM_{10}}^b = \rho_d[P_{10} + P_{2.5} + 1.375S + 1.8(OC_1 + OC_2)$$

229
$$+BC_1 + BC_2 + D_1 + 0.286D_2 + D_3 + 0.87D_4 + S_1 + 0.942S_2 + S_3]$$

230   where P_{10} is coarse unspecified aerosol contributions, D_3 and D_4 are dusts with

231   effective radii of 2.4 and 4.5 μm. S_3 is sea salt with effective radii of 3.2 μm. Therefore, the

232   simulated $PM_{10\text{-}2.5}$ is:

233
$$y_{PM_{10-2.5}}^b = \rho_d[P_{10} + D_3 + 0.87D_4 + S_3]$$

234   In this research, $y_{PM_{10-2.5}}^o$ calculated by $y_{PM_{10}}^o - y_{PM_{2.5}}^o$ is used to analyze state variables

235   including D_5 and S_4, which are dust with effective radii of 8 μm and sea salt with effective

236   radii of 7.5 μm, respectively.

237   2.3 Site observation data and errors

238   Ground-based observation features high temporal resolution, which can capture variation

239   of pollution concentration on an hourly scale at the bottom of the troposphere, providing

240   continuous and reliable observation. The quality-assure and quality-controlled hourly

241   observation data of $PM_{2.5}$ and PM_{10} are used to explore the influence of 4D-LETKF assimilation

242 in this research. The pollution data was obtained from China National Environmental

243 Monitoring Center (http://106.37.208.233:20035/). As the research primarily focuses on the

244 BTH region, the assimilation and verification sites are mainly located in the BTH region and

245 neighboring provinces, primarily located in urban and suburban areas. In order to obtain more

246 reliable observation data, the quality control of observation data in this study includes hourly

247 observation of default value and extreme value detection. First, during the haze period, if the

248 number of missing values for either type of pollutant at one site exceeds 24 hours, this site is

249 considered to have a certain uncertainty on observation quality, and data will not be assimilated.

250 Second, for each kind of observation in different station, the hourly observation outside the

251 range of m $\pm3\sigma$ will not be assimilated, where the m and σ denote the mean value and standard

252 deviation of daily time series, respectively. When selecting assimilation and verification sites,

253 spatial distribution uniformity is ensured for better assimilation performance, consequently,

254 those sites are randomly selected. Finally, 127 assimilation sites and 69 verification sites in the

255 BTH region and surrounding province are selected (Figure 1b). It can be seen that the

256 assimilation and verification sites have a relatively uniform spatial distribution.

257 The observation error covariance matrix (R) is assumed to be diagonal, implying that

258 observational errors among each pollution species are uncorrelated. The observation error (r)

259 consists of measurement error (ε_0) and representation error (ε_r):

$$r = \sqrt{\varepsilon_0^2 + \varepsilon_r^2}$$

260

261 The measurement error ε_0 is defined as:

$$\varepsilon_0 = ermax + 0.0075 * \Pi_0$$

262

263 where ermax is the base error, which is set to be 1 for $PM_{2.5}$, and PM_{10} (Chen et al., 2019a),

264   Π_0 denotes the observation of concentration. Produced by observation operator,

265   representativeness errors can be calculated by the formula (Elbern et al., 2007):

266 $$\varepsilon_r = \gamma\, \varepsilon_0 \sqrt{\Delta l / L}$$

267   γ is tunable scaling factor and 0.5 is set for γ, Δl is the spatial resolution of gridding (30 km

268   and 10km for d01 and d02, respectively), L depends on station location, which denotes the

269   range that an observation can reflect, here L is 2 km for calculation.

270   Meteorological data were collected from National Climatic Data Center

271   (https://wwww.ncei.noaa.gov/), which provides hourly air temperature, dew point, and

272   windspeed data. The observational meteorological data are used to validate the performance of

273   simulations in this study.

274   2.4 Experiment design

275   A series of control and data assimilation experiments during severe and moderate haze

276   events, as listed in Table 2, have been carried out to achieve our major objective. The control

277   experiments refer to numerical experiments without data assimilation. The Severe-FR

278   experiment with 48 hours spin up time is performed firstly to quantify the necessity of adjusting

279   particulate matter concentration during severe haze event. Severe-FR-24h, Severe-FR-48h, and

280   Severe-FR-72h accompany with restart every 24, 48, and 72 hours respectively and update

281   meteorological boundary conditions. Except Severe-FR, the rest of the experiments all have 24

282   hours of spin up time at the beginning of each restart or assimilation cycle. The settings of

283   assimilation experiments cycle time are same with corresponding control experiments. The

284   detail descriptions of experiment cycle time are shown in Figure S1. Since the effectiveness of

285   4D-LETKF is highly related with ensemble member size and length of assimilation window

286 (Rubin et al., 2016), the sensitivity analysis is employed to investigate the influence from two

287 parameters on assimilation effect (Kong et al., 2023). The selection of assimilation parameters

288 for the sensitivity experiments includes 20, 40 and 60 for ensemble members, and 24, 48 and

289 72 hours for the length of assimilation window empirically (Kong et al., 2021, Dai et al., 2021).

290 All sensitivity experiments use identical WRF-Chem physical parameterizations,

291 anthropogenic emission and random perturbations. Through the comparison between all

292 assimilation experiments, the influence rules of 4D-LETKF assimilation on the simulation of

293 particulate matter in severe haze can be retrieved. Lastly, aiming to determinate the applicable

294 range of obtained influence rules above, two assimilation experiments in a moderate haze event

295 are performed to validate whether the rules are also suitable to a less-polluted environment. The

296 detail reasons for selection of parameters will be fully described in the next section.

297 Table 2. design of numerical experiments in this research.

	Experiment	Design of simulation
Control experiments	Severe-FR	Free run experiment in severe haze event and without restart in integration process.
	Severe-FR-24h	Free run experiment in severe haze event and with restart every 24, 48 and 72 hours, provide deterministic simulation corresponding to data assimilation experiment.
	Severe-FR-48h	
	Severe-FR-72h	
	Moderate-FR-48h	Free run experiment in moderate haze events and with restart every 48 hours, provide deterministic simulation corresponding to data assimilation

		experiment.
Data assimilation experiments in severe haze event	Severe-20m-24h Severe-20m-48h Severe-20m-72h	Assimilation experiment in severe haze event with 20 ensemble members and 24, 48, 72 hours of assimilation window length respectively.
	Severe-40m-24h Severe-40m-48h Severe-40m-72h	Assimilation experiment in severe haze event with 40 ensemble members and 24, 48, 72 hours of assimilation window length respectively.
	Severe-60m-24h Severe-60m-48h Severe-60m-72h	Assimilation experiment in severe haze event with 60 ensemble members and 24, 48, 72 hours of assimilation window length respectively.
Data assimilation experiments in moderate haze event	Moderate-20m-48h Moderate-40m-48h	Assimilation experiment in moderate haze event with 20 and 40 ensemble members combine with 48 hours of assimilation window length.

298   Root mean square error (RMSE), mean errors (BIAS), mean absolute error (MAE) and

299 correlation coefficient are calculated in this study to evaluate the performance of each numerical

300 experiment. The assimilation efficiency (AE) for estimating the data assimilation performance

301 is also calculated from the formulation below (Yumimoto and Takemura, 2011):

302
$$AE = \frac{RMSE^f - RMSE^a}{RMSE^f} \times 100\%$$

303 where $RMSE^a$ and $RMSE^f$ is RMSE with and without assimilation, respectively. According

304 to the definition, if AE is positive, it means that RMSE has decreased due to assimilation effect.

305   When AE is equal to 1, RMSE in analysis completely disappears, and analysis is equal to

306   observation. The formulations of correlation coefficient and root mean square error are shown in

307   supplement.

308   3.   Results

309   3.1 Comparison of the analysis with control experiment

310   3.1.1 The reproduction of the severe haze event in BTH

311   It is essential to discuss the basic evolution of pollutant and the necessity of pollutant data

312   assimilation in severe haze event before conducting the assimilation experiments. The severe

313   haze event selected in this study occurred from 00:00 UTC 15 January 2020 to 00:00 UTC 21.

314   The AQI is a comprehensive indictor of overall air pollution and criterion for severe haze events

315   (Zhan et al., 2018, Bao et al., 2015). As a result, Figure 3(a) shows the temporal variation of

316   AQI at the six sites among BTH region during the investigated period. The peak value of AQI

317   mainly appeared on 18 January, and then rapidly decreased on 19 and 20 January. The temporal

318   averaged of AQI have exceeded 200, with particulate matter identified as the primary pollutant.

319   Fig. 3(b) provides the correlation coefficients and standardized standard deviations of five

320   parameters from Severe-FR against observations. Meteorological variables including air

321   temperature, dew point temperature and wind speed are well simulated when compared with

322    $PM_{2.5}$ and PM_{10}. The correlation coefficients of meteorological factors are all larger than 0.6,

323   while that of pollutant concentrations are all below 0.4. Therefore, when the meteorological

324   conditions can be retrieved relatively accurately, particulate matter assimilation is the key to

325   improving the simulative skill of pollutants.

326

327
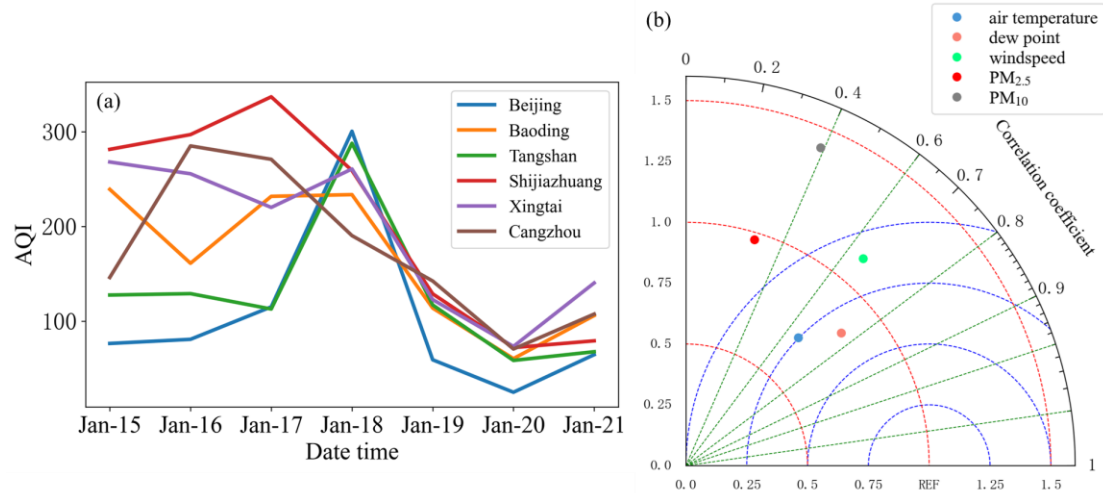
Figure3. (a) Temporal variation about AQI at six sites in severe haze event. (b) A Taylor graph

describing simulation from Severe-FR about five kinds of parameters compared with the

observed ones in BTH region.

3.1.2 The improvement in the reproduction of severe haze achieved by 4D-LETKF

The divergence between assimilation and control experiment reflects the contribution from

4D-LETKF initial condition adjustment. Consequently, the study takes an ensemble member

size of 40 and assimilation window length of 48 hours to conduct sensitivity experiment and

compare with Severe-FR-48h which has the same integration time in each cycle to validate the

effectiveness of 4D-LETKF assimilation system (the analysis from the selection of 40 ensemble

members and 48 hours of assimilation window length is presented here because it shows the

best performance among sensitivity experiments in the next section). Figure 4 reveals the

performance of control and assimilation experiments in severe haze event. The RMSE values

of $PM_{2.5}$ and PM_{10} in Severe-FR-48h are 69.93 and 106.88μg m^{-3} and both with scattered

distribution, indicating substantial uncertainty exist in reproducing this severe haze event. In

Severe-40m-48h, the RMSE values of $PM_{2.5}$ and PM_{10} are 31.19 and 76.83μg m^{-3}, decreasing

by 55.40% and 28.12% respectively in a high particulate matter concentration environment.

344   The decreased RMSE values also imply that the assimilation system has reached a well-

345   calibrated stage. Not only more points are getting together, but smaller simulation errors for

346    $PM_{2.5}$ and PM_{10} also imply that the Severe-40m-48h outperforms the Severe-FR-48h in this

347   severe haze event.

348
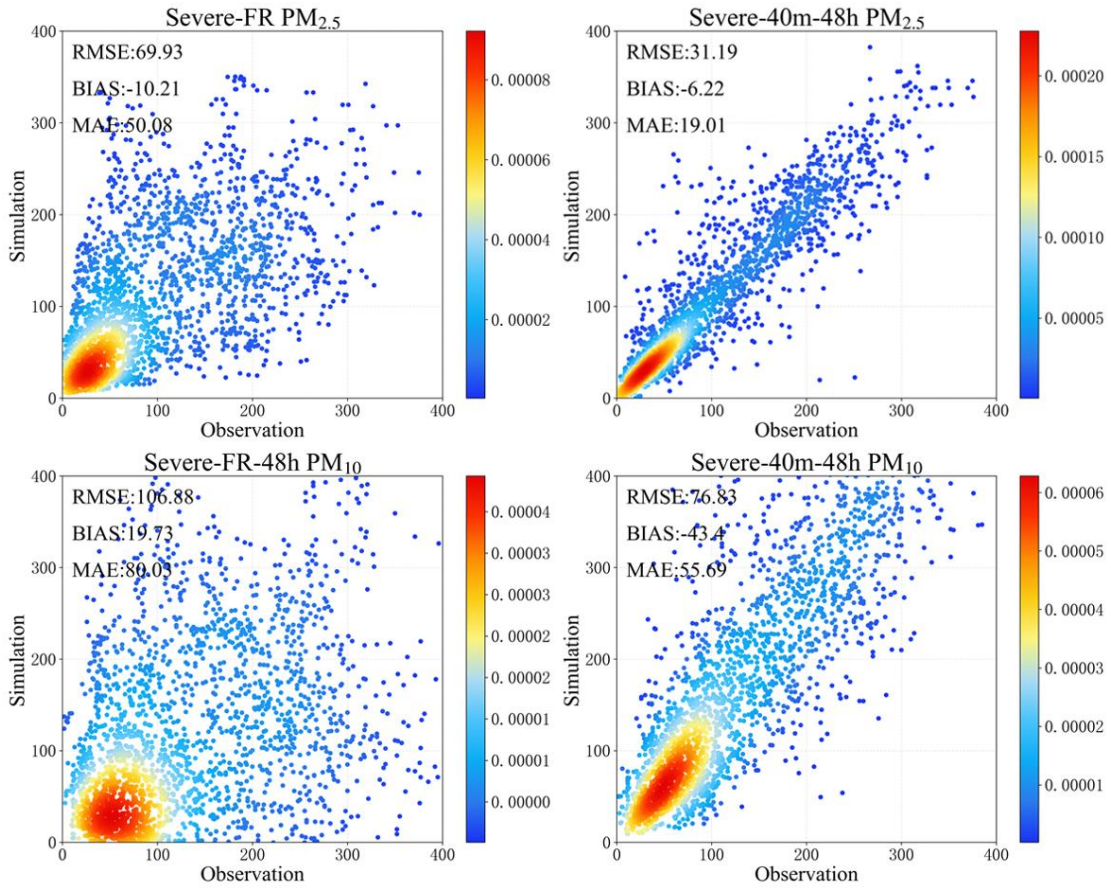
349   Figure 4. Scatter and density plot of $PM_{2.5}$ and PM_{10} in Severe-FR-48h and Severe-40m-

350   48h versus observations from verification stations (units: µg m^{-3}). The color bar represents the

351   Gaussian Kernel Density estimation.

352   In order to acquire basis distribution of simulation errors for particulate matter, Figure 5

353   presents the frequency distribution of deviations between observed and simulated particulate

354   matter concentrations in Sevre-FR-48 and Severe-40m-48h experiments. It is obviously that

355   Severe-40m-48h increases the frequency of low deviations and decrease those of high

356 deviations in the simulation of $PM_{2.5}$. The deviation pattern of $PM_{2.5}$ in Severe-40m-48h is

357 generally squeezed with higher peaking and symmetrical to the value of 0 than Severe-FR-48h.

358 For the deviation distribution pattern of PM_{10}, it shows high frequency of negative deviations

359 and great underestimation in the Severe-FR-48h, and this underestimation has been effectively

360 corrected by the adjustment of initial conditions and step analysis in Severe-40m-48h. Specially,

361 the proportion of deviation within 20 μg m^{-3}in the Severe-40m-48h is 69.98% for $PM_{2.5}$ and

362 31.90% for PM_{10}.

363
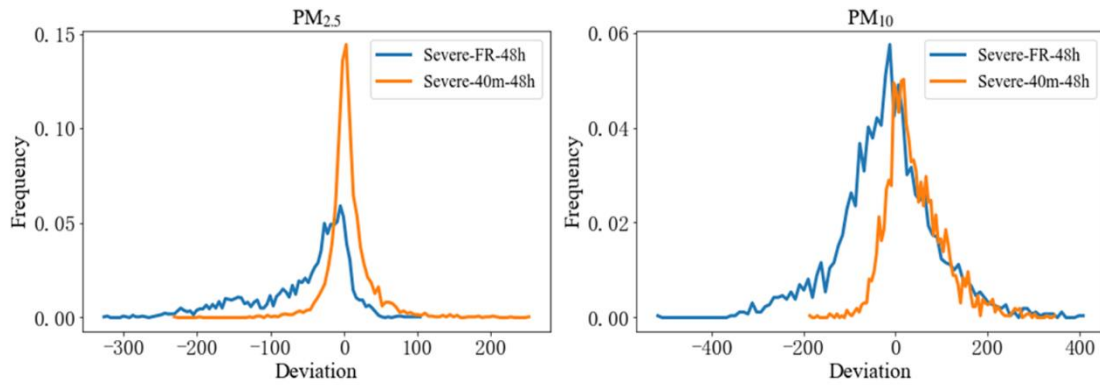
364 Figure 5. Frequency distribution of the deviations about the simulated $PM_{2.5}$ and PM_{10}

365 concentrations in Severe-40m-48h and Severe-FR-48h minus the observed ones (units for

366 deviation: μg m^{-3}).

367 Figure 6 exhibits the spatial distribution of four statistical parameters about RMSE for

368 particulate matter among the BTH region. By comparison from the Severe-FR-48h and Severe-

369 40m-48h, there are significant RMSE reduction for $PM_{2.5}$ after assimilation, implying that the

370 actual evolution of $PM_{2.5}$ can be better represented by Severe-40m-48h. For instance, the RMSE

371 values of $PM_{2.5}$ in Baoding, Hengshui and Cangzhou, have significantly decreased to 29.85,

372 18.98, and 19.06μg m^{-3}, respectively, compared to 80.55, 55.22 and 76.32 μg m^{-3}in the Severe-

373 FR-48h. AE in most verification stations has exceeded 50% also suggests the high efficiency

374   of 4D-LETKF assimilation for the simulation of $PM_{2.5}$. Although the performance of

375   assimilation experiment in Shijiazhuang city does not have a good agreement with observation

376   and shows a positive difference, high values of AE in most of verification stations also proves

377   the validation of assimilating effect for PM_{10}. Compared to the Severe-FR-48h, the Severe-

378   40m-48h productively reduces the RMSE of PM_{10}, accompany with high values of 61.18%,

379   59.17% and 52.18% about AE on Zhangjiakou, Tangshan and Hengshui, respectively.

380
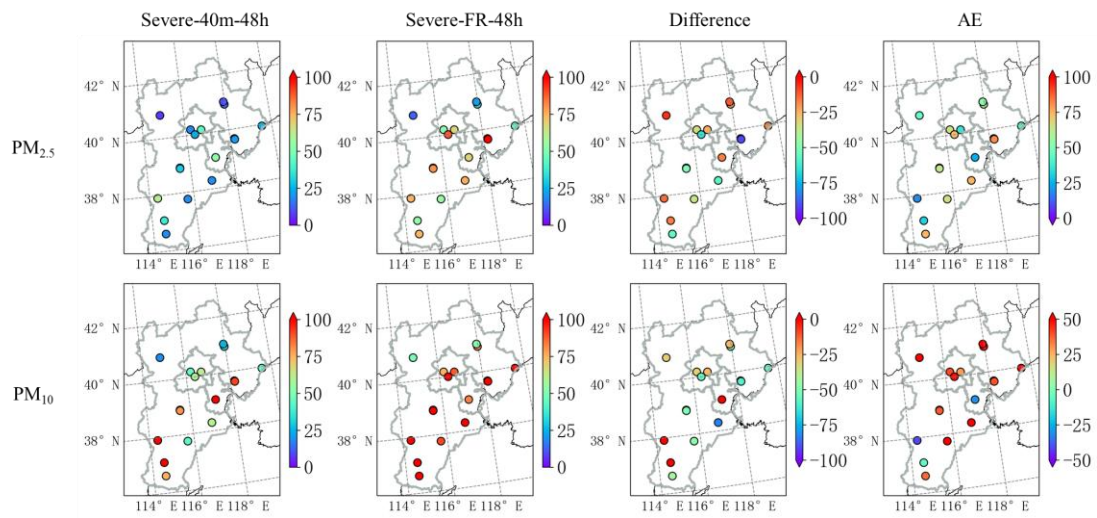
381   Figure 6. Spatial distribution of RMSE values from Severe-40m-48h (first column), Severe-

382   FR-48h (second column), their difference (third column) and AE (fourth column) for $PM_{2.5}$

383   (first row) and PM_{10} (second row) from 15 January to 21 January among verification station

384   in BTH region. The difference implies the RMSE in Severe-40m-48h minus those in Severe-

385   FR-48h (units: $\mu g\ m^{-3}$). AE is assimilation efficiency and has been described in methodology

386   before. The grey border implies the BTH region.

387   The spatial distribution of correlation coefficients from Severe-40m-48h, Severe-FR-48h,

388   their difference for $PM_{2.5}$ and PM_{10} are also illustrated in Figure 7. The assimilation experiment

389   increases the correlation coefficients to more than 0.6 at all sites in the simulations of $PM_{2.5}$ and

390   exceed 0.7 among the southern BTH region in the simulations of PM_{10}. The Severe-40m-48h

391 also reverses the opposite trend of PM$_{2.5}$ and PM$_{10}$ series in Severe-FR-48h versus observations,

392 for example, the correlation coefficients in Severe-FR-48h at Chengde and Zhangjiakou are -

393 0.42 and -0.53, but increase to 0.52 and 0.69 after assimilation in the simulations of PM$_{10}$.

394 Incorporating more assimilable observations may further increase the correlation coefficient in

395 the simulation of particulate matter (Kong et al., 2021). Data assimilation by multiple

396 observations from diverse platform is necessary because it can integrate and coordinate

397 observational information into aerosol forecasts well and then improve air pollutant forecast

398 accuracy (Barbu et al., 2009, Ma et al., 2020).

399
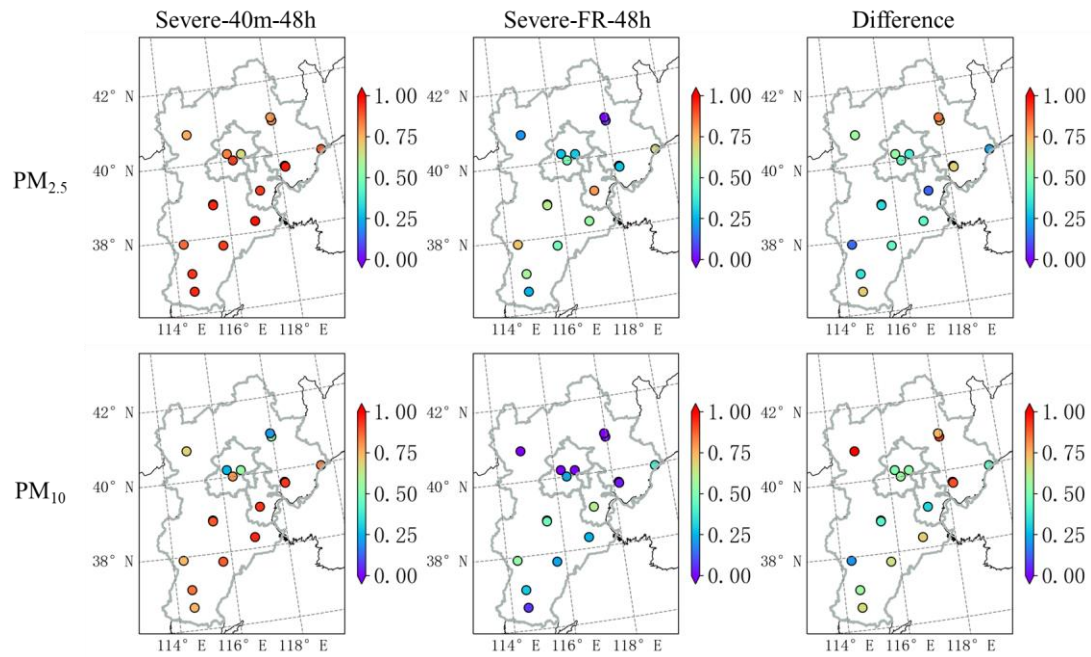
401 Figure 7. Spatial distribution of correlation coefficients from Severe-40m-48h (first column),

402 Severe-FR-48h (second column), their difference (third column) for PM$_{2.5}$ (first row) and

403 PM$_{10}$ (second row) from 15 January to 21 January among verification station in BTH region.

404 The difference implies the correlation coefficient in Severe-40m-48h minus those in Severe-

405   FR-48h. The grey border implies the BTH region.

The temporal variations of particulate matter from Severe-40m-48h, Severe-FR-48h and observation at six independent verification stations are shown in Figure S2 and Figure S3. The six independent verification stations have experienced different levels of air pollution and distributed uniformly over BTH region. It is apparently that the analysis at six stations have good agreement with observations both for $PM_{2.5}$ and PM_{10}, which can better characterize the peaks and valleys of particulate matter concentration over investigated period.

Table 3 lists the $\triangle$ RMSE, $\triangle$ CORR and AE in the simulations of particulate matter at independent stations outside the BTH region. The RMSEs and correlation coefficients have decreased and increased respectively after assimilate ground-based observations, suggesting that the uncertainty in Severe-FR-48h has been well optimized not only in the BTH region, but also includes the whole simulation domain. The main source of these gains is generated from local initial field assimilation. Compared to the Severe-FR-48h, the analysis in Yuncheng shows that the RMSE values of $PM_{2.5}$ and PM_{10} have decreased by 98.26 and 144.56 $\mu g\,m^{-3}$ remarkably, such a great improvement may relate to the enhanced estimation capability about state variables of particulate matter. The high values of AE also suggest that verification observation sites outside the BTH region have achieved a good Kalman gain. In previous researches, predicting heavy haze events in northern China, especially over the BTH Region, remained a challenge when compared to other regions like Pearl River Delta and Yangtze River Delta in China (Feng et al., 2018, Gao et al., 2017). In this research, the analysis is propagated by meteorological elements including temperature, air pressure and wind fields come from NCEP Final analysis data, which may provide an optimal meteorological boundary conditions for the assimilation of pollutant concentration.

428   Table 3. Statistics about PM$_{2.5}$ and PM$_{10}$ from analysis in the cities among neighboring

429   provinces of BTH region. Δ RMSE (Δ CORR) represent the RMSE (correlation coefficient)

430   from analysis minus those from Severe-FR-48h (units for Δ RMSE: μg m^{-3}).

City/ Statistical variable	PM$_{2.5}$			PM$_{10}$		
	Δ RMSE	Δ CORR	AE	Δ RMSE	Δ CORR	AE
Taiyuan	-21.30	+0.41	23.93%	-54.8	+0.71	39.05%
Changzhi	-38.39	+0.38	65.93%	-63.06	+0.68	63.22%
Jincheng	-37.94	+0.37	66.85%	-94.32	+0.89	72.45%
Shuozhou	-27.07	+0.31	58.96%	-100.08	+0.84	69.96%
Yuncheng	-98.26	+0.67	77.85%	-144.56	+1.25	80.64%
Hohhot	-92.30	+0.67	74.53%	-121.79	+1.41	68.92%
Chifeng	-16.90	+0.55	64.95%	-38.18	+0.95	60.85%
Huludao	-38.56	+0.20	59.11%	-95.95	+1.04	65.76%
Jinzhou	-42.97	+0.21	61.17%	-46.26	+0.83	45.83%
Chaoyang	-39.37	+0.37	51.14%	-83.04	+1.23	61.86%
Jinan	-44.90	+0.63	69.71%	-71.22	+0.59	62.93%
Qingdao	-23.99	+0.27	37.98%	-72.05	+0.44	72.21%
Shouguang	-28.70	+0.21	58.03%	-48.92	+0.39	47.57%
Anyang	-35.87	+0.41	62.53%	-32.08	+0.60	33.15%
Zhengzhou	-26.26	+0.37	37.51%	-3.64	+0.42	3.73%

431   3.2 The sensitivity of 4D-LETKF to ensemble member size and length of assimilation

432 window

433   In previous section, the research has compared the performance from assimilation

434 experiment with 40 ensemble members and 48 hours of assimilation window length against that

435 do not integrate hourly pollutant observations. The results fully demonstrate the ability of 4D-

436 LETKF assimilation method to reproduce severe haze events in spatial and temporal

437 dimensions. However, the 4D-LETKF assimilation effect is highly rely on selection of

438 ensemble member size and length of assimilation window, so how does the assimilation

439 approach vary to the parameterized selection in severe haze event? It is of great meaning to

440 conduct sensitivity experiments based on ensemble member size and length of assimilation

441 window, compare each performance of them by statistical metrics, and summarize the general

442 influence rule of 4D-LETKF parameter selection. Consequently, nine panels of sensitivity

443 experiments are conducted with the selection of ensemble member size (20, 40, 60 members)

444 and the length of assimilation window (24, 48, 72 hours) to maximize the positive innovation

445 in this section.

446   Figure 8 reveals the heatmap about RMSE in each sensitivity experiment of particulate

447 matter over verification sites among the BTH region. The results of free run experiment with

448 different integration times (24, 48, 72 hours) are offered here for comparison with analysis

449 which with same assimilation cycle time. The RMSEs of $PM_{2.5}$ and PM_{10} in each free run

450 experiment exceed 60μg m^{-3} and 100μg m^{-3}, respectively. It is apparently that the 4D-LETKF

451 performs better than the FR experiment in the simulation about $PM_{2.5}$ and PM_{10} over wide range

452 of ensemble member sizes and assimilation window lengths, illustrating the broad applicability

453 of 4D-LETKF data assimilation to these parameters. However, it can be found that the analysis

454   of $PM_{2.5}$ and PM_{10} are dependent on length of assimilation window and dramatically related to

455   ensemble member size in all sensitivity experiments. Unlike the short-lived and chemical

456   reactive species (such as SO_2 and NO_2) which easily undergo complex and nonlinear

457   photochemical reactions, a relative longer assimilation window length seems more suitable for

458   assimilating ground-based particulate matter observations (Peng et al., 2017, Kong et al., 2021).

459   A longer assimilation window length could also avoid underestimation of model spread, which

460   implies overconfidence in the first guess state estimate by enough integration time of each

461   member (Schutgens et al., 2010, Miyazaki et al., 2012a, Hunt et al., 2007). Hence, 48 or 72

462   hours of assimilation window length are advised to optimize the ensemble concentration

463   trajectories. On the other hands, increasing ensemble member size efficiently reduces

464   uncertainty in $PM_{2.5}$ and PM_{10}, as evidenced by the decrease of RMSEs from free run to

465   assimilation experiments with 20 and 40 members. However, when compared with the results

466   from 40 ensemble members, the accuracy of numerical simulations has not significantly

467   improved for both $PM_{2.5}$ and PM_{10} with 60 ensemble members, indicating that 40 members are

468   sufficient and feasible to provide a reliable estimation of the background error and analysis

469   rather than more numerical source consumption. Considering numerical source consumption

470   and RMSE values in the simulations of $PM_{2.5}$ and PM_{10}, the Severe-40m-48h shows more

471   comparable to the observations when compared with the other eight panels of sensitivity
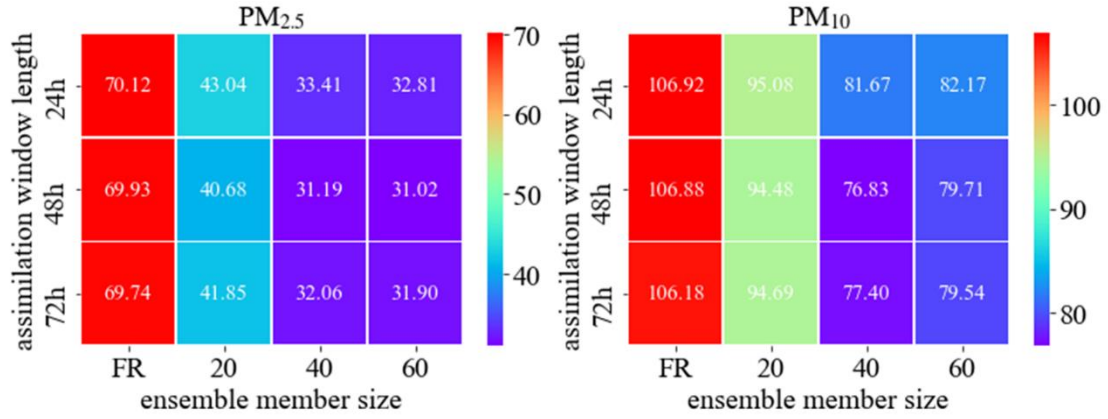
472   experiments.

Figure 8. Heatmap about RMSE in each sensitivity experiment of particulate matter over

verification sites (units: μg m^{-3}). The number in each small square represents the RMSE

between observation and simulation for each combination of ensemble member size and the

length of assimilation window methods.

3.3 The influence from ensemble member size to the ensemble spread

In order to explore why increasing ensemble member size can efficiently reduce the

uncertainty in the analysis of PM$_{2.5}$ and PM$_{10}$ as revealed in Figure 8, the study investigates the

spatial distribution of standard deviations of PM$_{2.5}$ and PM$_{10-2.5}$ among first guess ($x^b(i)$) and

analysis field ($x^a(i)$) in terms of ensemble members. The standard deviations of ensemble

members describe how the emission perturbation propagates among the forward model, and

this perturbation is driven by the underlying surface pollution emission inputs and the

meteorological conditions. Therefore, the standard deviation in the first guess fields quantifies

the dispersion degree of the ensemble background, substantially impacts the calculation of

assimilation parameters such as ensemble state vector perturbations, and further affects the

performance of particulate matter predictions.

Since the RMSE decreases with the increasing ensemble member size when 20 and 40

members are setting, and 48 hours of assimilation window length corresponds to a smaller

491 RMSE, the study compares the spatial distribution of ensemble standard deviations from

492 Severe-20m-48h and Severe-40m-48h to explain the relationship between ensemble member

493 size and simulation errors in analysis result. Figure 9 depicts contour maps of the spatial

494 distribution of temporal averaged standard deviations in the first guess and analysis of Severe-

495 40m-48h, Severe-20m-48h and their difference for $PM_{2.5}$ and $PM_{10-2.5}$ during severe haze event.

496 The first guess in Severe-40m-48h and Severe-20m-48h shows that the relatively high standard

497 deviations are generally observed in southern of BTH region, while those in the northern areas

498 are close to zero for both $PM_{2.5}$ and $PM_{10-2.5}$. High value centers are distributed in densely

499 populated areas and urban centers including Shijiazhuang, Xingtai, Tianjin and Tangshan city,

500 where the standard deviations have generally exceeded $30\mu g\ m^{-3}$. Combined with Figure S4, it

501 can be seen that the areas with large concentration standard deviations correspond well with the

502 spatial distribution of anthropogenic emission and the areas with large standard deviations of

503 emission sources. The standard deviations of concentrations of $PM_{2.5}$ and $PM_{10-2.5}$ have closely

504 relationship with the allocation and configuration of anthropogenic emission sources, because

505 disturbances are only added to emission sources for each ensemble member, without disturbing

506 the meteorological field in this haze event. The variation of difference in the third column

507 entirely comes from increasing ensemble member size. The positive difference between Severe-

508 40m-48h and Severe-20m-48h in first guess suggests that increasing ensemble member size

509 leads to greater differences among each ensemble for both $PM_{2.5}$ and $PM_{10-2.5}$ over BTH areas.

510 The high efficiency of 4D-LETKF is strongly influenced by sufficient information spread

511 among ensemble members, which integrate spreading observational information to produce

512 analysis from the first guess (Rubin et al., 2016). As a result, the increasing ensemble member

513   size improves divergence for each member and facilitates the state vectors about $PM_{2.5}$ and

514    $PM_{10\text{-}2.5}$ information spread in the first guess, which makes a better performance for Severe-

515   40m-48h rather than Severe-20m-48h in this severe haze event. The standard deviations of

516    $PM_{2.5}$ in analysis are generally lower than those in first guess. Due to the localization of 4D-

517   LETKF, that is the ground-based observation data only optimized for simulation grid within a

518   certain range, square-like areas of low standard deviations appear in the analysis of $PM_{2.5}$ both

519   for 40 and 20 ensemble members. Nearly all assimilated stations are located at the center of

520   low value square areas suggesting that 4D-LETKF tunes all $PM_{2.5}$ trajectories into a small range

521   with low standard deviation at each slot of analysis by the assimilation of ground-based

522   observations. For $PM_{10\text{-}2.5}$, there are no square-like areas of low standard deviations in the

523   analysis both for 40 and 20 ensemble members, indicating that the 4D-LETKF does not has an

524   obvious limitation for $PM_{10\text{-}2.5}$ trajectories, however, the decreased standard deviations effect

525   from the 4D-LETKF is still distinct for the particulate matter because PM_{10} consist of $PM_{2.5}$

526   and $PM_{10\text{-}2.5}$ in simulation. Enlarging ensemble member size is benefit to the improving of

527   standard deviations of $PM_{2.5}$ and $PM_{10\text{-}2.5}$ in analysis, while the improving magnitude of $PM_{2.5}$

528   is obviously smaller than $PM_{10\text{-}2.5}$. The assimilation results are not directly influenced by the

529   increased standard deviations in analysis. Such low increasement of standard deviations

530   (generally below 3 $\mu g\ m^{-3}$) is unlikely to induce uncertainty in the fitting and averaging process,

531   but facilitates divergence in initial conditions between forecasting members in the next

532   assimilation cycle. In addition, Figure S5 depict the spatial distribution of standard deviation

533   from Severe-60m-48h, Severe-20m-48h and their difference in the first guess and analysis field.

534   It can be seen that increasing the number of ensemble member generally also improves the

standard deviation in first guess and analysis over the BTH region both for $PM_{2.5}$ and $PM_{10-2.5}$.

Overall, the increasement of standard deviations generated by increasing ensemble member

size directly improves the information spread of ensemble members in the first guess field and

the assimilation effect of 4D-LETKF, while the positive difference of standard deviation in

analysis favors the variances between each initial condition in the next assimilation window

during severe haze event.
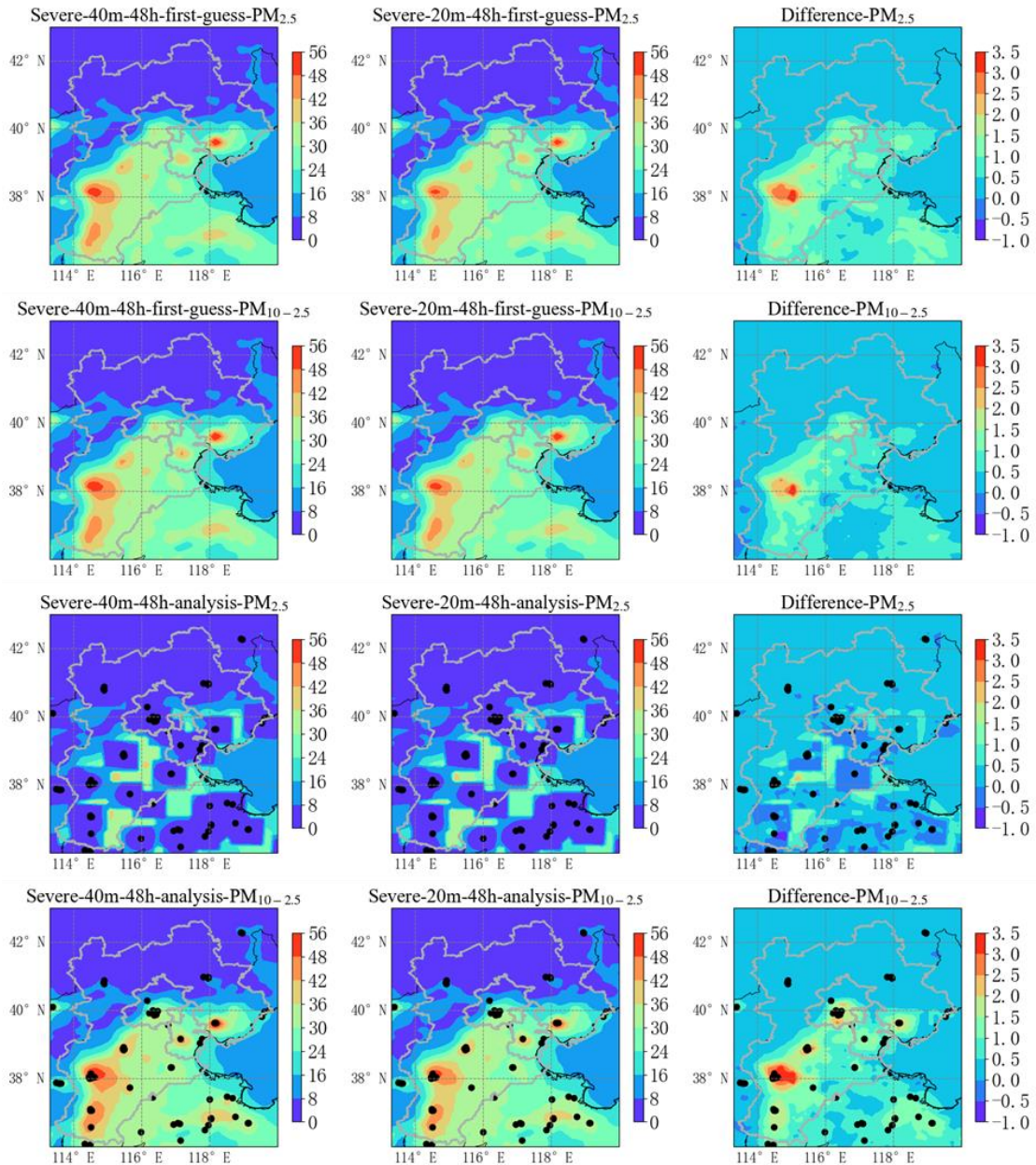
543   Figure 9. Contour maps of spatial distributions of temporal averaged $PM_{2.5}$ and $PM_{10\text{-}2.5}$

544   standard deviations in the first guess (first and second row) and analysis (third and fourth

545   row) of Severe-40m-48h, Severe-20m-48h and their difference (Severe-40m-48h minus

546   Severe-20m-48h) within simulation period (units: $\mu g\ m^{-3}$). The black dots in analysis of $PM_{2.5}$

547   and $PM_{10\text{-}2.5}$ implies the location of assimilated stations. The grey border implies the BTH

548   region.

549   In the other sides, no matter for the first guess from Severe-40m-48h or Severe-20m-48h,

550   the high standard deviations are found near Shijiazhuang region in Figure 9, but Shijiazhuang

551   station (37.91N°, 114.35°E) still with larger RMSE and smaller AE in Figure 6. This seems

552   contrary to the opinion that increasing standard deviations in the first-guess field is beneficial

553   to raising the accuracy of pollutant simulations. Therefore, Shijiazhuang station and the stations

554   which with high values of AE (exceed 50) and difference of standard deviation in first guess

555   (exceed 1 $\mu g\ m^{-3}$) including Beijing, Tangshan, Handan, Baoding, Cangzhou, and Hengshui

556   regions are selected to explore the temporal distribution of standard deviations difference

557   between 40 and 20 ensemble members, so as to further advance our understanding about the

558   relationship between ensemble member size and simulation uncertainty in 4D-LETKF system.

559   The geographical locations of observations are shown in Figure S6 of the supplement. Figure

560   10 examines the temporal distribution of the standard deviation difference for $PM_{2.5}$ and $PM_{10\text{-}2.5}$

561    $_{2.5}$ during the investigated period at Shijiazhuang station and results averaged from the selected

562   stations. From January 17 to January 18, the standard deviation difference in first guess at

563   Shijiazhuang station has increased drastically and exceeded up to 10 $\mu g\ m^{-3}$ for both $PM_{2.5}$ and

564    $PM_{10\text{-}2.5}$. This uneven temporal distribution results in a large standard deviation difference of

first guess in Figure 9. This huge divergency between ensemble member may attributed to the peak pollutant levels with AQI exceeds 300 at Shijiazhuang station occurs on the January 17 as shown in Figure 3. In highly polluted environments, 40 forecasting members with different perturbations in emission sources are more likely to differ the concentration of particulate matter in first guess fields. Excessive large spread of $PM_{2.5}$ and $PM_{10-2.5}$ for ensemble members may arise an over-high estimation about background error variance and obtain a poor Kalman gain. Moreover, it can be found that the standard deviation difference of $PM_{2.5}$ and $PM_{10-2.5}$ at Shijiazhuang station are obviously lower than the averaged from selected stations except the high dispersion time, suggesting the increasing number of ensemble members has limited impact on the spread between each ensemble member at Shijiazhuang during these dates. Too low standard deviations imply filter divergence near Shijiazhuang station, which may induce the underestimation of model spread, reduce the effect of observation information, and make system more certain of state estimate about particulate matter concentrations in first guess (Hunt et al., 2007). In addition, reducing uncertainty in the mixed anthropogenic emission inventory may be an important approach to avoid filter convergence near the Shijiazhuang region. Generally edited by empirical and statistical data such as anthropogenic emission factors and activity dataset, the anthropogenic emissions based on bottom-up method can hardly capture the real spatiotemporal distribution of anthropogenic emissions over China as frequently variations in energy consumption, even though the latest version. Among the southern of BTH region, the great positive innovations of particulate matter emissions in posterior estimation have been discovered in previous researches, implying that the update of underestimated emissions in this region may enlarge ensemble spread since a large quantity of

587 emissions corresponds to a higher degree of perturbation (Peng et al., 2017, Feng et al., 2023).

588 In a word, the perturbations added to emissions and meteorological fields needs to be executed

589 carefully in 4D-LETKF system to avoid too high or too low ensemble spread degree because

590 which determinate how analysis results weight toward observations information and first guess

591 fields (Dai et al., 2021).

592
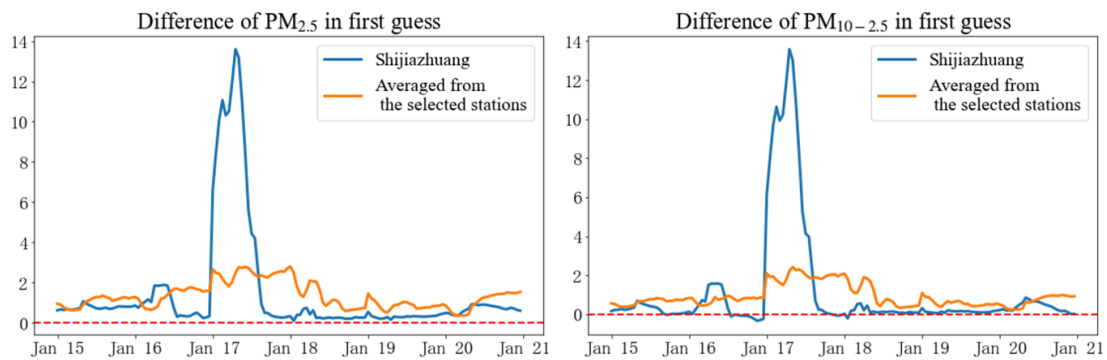
593 Figure 10. Temporal distribution of standard deviation difference (Severe-40m-48h minus

594 Severe-20m-48h) in first guess for $PM_{2.5}$ and $PM_{10-2.5}$ at Shijiazhuang station and averaged

595 from the selected stations (units: $\mu g\ m^{-3}$). The red dash line is zero.

596 The results above suggest that the increasing ensemble member size enlarges ensemble

597 spread, benefits the information spread in the first guess and finally improves the simulative

598 skill in severe haze event. However, it has not been testified whether these influence rules are

599 also practical for a more common, and less polluted condition. Therefore, two assimilation

600 experiments in moderate haze event, Moderate-20m-48h and Moderate-40m-48h, are

601 performed to examine the applicable range. As shown in Figure S7, the moderate haze event

602 spans from 00:00 UTC 15 January 2019 to 00:00 UTC 21. This moderate event began on 15

603 January, with AQI increasing until 18 January, reaching a moderate level but not lasting for a

604 long time, and then decreased on 19 and 20 January. Most areas experienced mild or moderate

605 air pollution, with AQI generally below 200, the primary pollutant was particulate matter after

calculation. The simulations of moderate haze event utilize the same anthropogenic emission

inventory as used in severe haze event since two events both happen in January, thereby avoids

the additional influence introduce from emission source variation and the perturbations to

information spread and assimilation effect.

Figure S8 shows the simulated concentrations of $PM_{2.5}$ and PM_{10} against ground-based

observations during moderate air pollution event. The RMSEs of $PM_{2.5}$ in Moderate-FR-48h,

Moderate-20m-48h and Moderate-40m-48h are 40.40, 24.12 and 18.52$\mu g\ m^{-3}$, respectively, and

the RMSEs of PM_{10} are 73.47, 67.81 and 57.04 $\mu g\ m^{-3}$ respectively. The concentrations of $PM_{2.5}$

and PM_{10} in assimilation experiments are more in agreement with observations, suggesting the

validation of 4D-LETKF initial condition adjustment in moderate haze event. The phenomena

that the simulation error of $PM_{2.5}$ and PM_{10} decrease with increasing ensemble member size are

same with those characteristics have shown in severe haze event before.

Similar to Figure 9, Figure S9 presents the spatial distributions of standard deviations about

$PM_{2.5}$ and PM_{10} in the first guess of Moderate-40m-48h, Moderate-20m-48h and their

difference. The relatively smaller magnitude of standard deviation difference in first guess may

relate to relatively low $PM_{2.5}$ and PM_{10} concentrations in moderate haze event. Positive

difference in first guess and analysis for particulate matter implies the Moderate-40m-48h

obtains a higher diversity of ensemble members than Moderate-20m-48h, and which are also

similar with those happen in the severe haze event.

4. Summary

The numerical reproduction of severe haze events with AQI larger than 200 has been a

challenging problem in the field of atmospheric pollution for a long time. In this research, a

628 WRF-Chem/4D-LETKF coupled data assimilation system has been successfully developed by

629 ensemble member with perturbed anthropogenic emissions to improve the simulative skill of

630 particulate matter in severe haze event during the winter of 2020. The research validated the

631 effectiveness of 4D-LETKF data assimilation, discussed the optimal parameter combination of

632 ensemble member size and length of assimilation window for 4D-LETKF assimilation system,

633 summarized and explained the influence rules from parametric selection to the 4D-LETKF

634 assimilation effect during severe and moderate haze event.

635   It is concluded that the Severe-40m-48h experiment shows the best performance in the

636 simulations of $PM_{2.5}$ and PM_{10} after comparing the statistical errors and computing resource

637 consumption across multiple sensitivity analyses, with the RMSEs of 31.19 and 76.83μg m^{-3}

638 for $PM_{2.5}$ and PM_{10} in severe haze event. Severe-40m-48h optimizes the underestimation of

639 particulate matter concentrations in Severe-FR-48h, and remarkably improves the simulation

640 accuracy in the entire BTH region and neighboring provinces. For example, the RMSEs of

641 $PM_{2.5}$ in Baoding, Hengshui and Cangzhou decrease to 29.85, 18.98 and 19.06 μg m^{-3}

642 respectively, from 80.55, 55.22 and 76.32 μg m^{-3} in Severe-FR-48h. Severe-40m-48h is also

643 capable of retrieving the peaks and valleys of particulate matter concentration over the

644 investigated period. To examine the dependence of the assimilation effect of 4D-LETKF, nine

645 panels of sensitivity tests were conducted according to ensemble member size and length of

646 assimilation window. The findings suggest that the simulation accuracy of $PM_{2.5}$ and PM_{10} can

647 be strongly improved by the increasing ensemble member size from 20 to 40. A relative longer

648 assimilation window length such as 48 or 72 hours combine with 40 ensemble member size is

649 advised in 4D-LETKF assimilation system. In view of performance of ensemble member,

650   increasing ensemble member size improves ensemble spread among each forecasting member,

651   facilitates the spread of state vectors about $PM_{2.5}$ and PM_{10} information in the first guess, favors

652   the variances between each initial condition in the next assimilation window and leads to better

653   performance in simulation of severe haze event. A similar conclusion can also be draw from the

654   moderate haze event, suggesting that this influence rule is applicable in both severe and

655   moderate haze conditions.

656   There are still some deficiencies in this research. Although we have performed data quality

657   control in this study, we did not use approaches such as super-observations to improving the

658   correspondence between grid points and observations (Jin et al., 2022, Miyazaki et al., 2012a),

659   which may increase the representational error and result in the possibility of two stations with

660   different concentrations interpolating in the same grid. Improving the spatial resolution of

661   forward model or introducing super observations may mitigate this problem (Miyazaki et al.,

662   2012b, Feng et al., 2020b). Furthermore, the concentration of state variables about particulate

663   matters in initial conditions are optimized in this study, but there still remain large uncertainties

664   in anthropogenic emission data, which is an important chemical boundary input for pollutant

665   simulations. These uncertainties sources may play a significant role in the over- or

666   underestimation of pollutant ensemble modeling. The anthropogenic emissions inversion based

667   on Ensemble Kalman filter and their variants is recognized as an effective approach for

668   reducing uncertainty in anthropogenic emission sources (Peng et al., 2018, Feng et al., 2020a,

669   Chen et al., 2019b). The jointly adjust initial conditions and emissions source with 4D-LETKF

670   is the focus of future work to further improving the forecast skills about air pollutants during

671   heavy pollution events.

672

CRediT authorship contribution statement

Jianyu Lin: Conceptualization, Formal analysis, Visualization. **Tie Dai**: Investigation, Methodology, Resources, Supervision. **LiFang Sheng**: Funding acquisition, Project administration. **Weihang Zhang**: Writing - original draft, Data curation. **Shangfei Hai**: Writing - review and editing. **Yawen Kong**: Validation.

Declaration of competing interest

The authors declare that they have no conflict of interest.

Acknowledgements

Financial support. This work is supported by the National Natural Science Foundation of China (No. 42275191), National Natural Science Funds of China (42375190).

Code and data availability

The code and data in this research are available in https://zenodo.org/records/14010521, and we are grateful to the relevant researchers who make contributions to WRF-Chem model and LETKF method (Miyoshi, 2024).

Reference

Anderson, J. L.: An adaptive covariance inflation error correction algorithm for ensemble filters,

Tellus, 59A, 210–224, https://doi.org/10.1111/j.1600-0870.2006.00216.x, 2007.

Anderson, J. L. and Anderson, S. L.: A Monte Carlo implementation of the nonlinear filtering problem to produce ensemble assimilations and forecasts, Mon. Weather Rev., 127, 2741–2758, 1999.

Bao, J., Yang, X., Zhao, Z., Wang, Z., Yu, C., Li, X.: The spatial-temporal characteristics of air pollution in China from 2001-2014, Int. J. Environ. Res. Publ. Health, 12 (12), 15875e15887, https://doi.org/10.3390/ijerph121215029, 2015.

Barbu, A. L., Segers, A. J., Schaap, M., Heemink, A. W., and Builtjes, P. J. H.: A multi-component data assimilation experiment directed to sulphur dioxide and sulphate over Europe, Atmospheric Environment, 43(9), 1622–1631, https://doi.org/10.1016/j.atmosenv.2008.12.005, 2009.

Benedetti, A., Morcrette, J., Boucher, O., Dethof, A., Engelen, R. J., Fisher, M., Flentje, H., Huneeus, N., Jones, L., Kaiser, J. W., Kinne, S., Mangold, A., Razinger, M., Simmons, A. J., and Suttie, M.: Aerosol analysis and forecast in the European Centre for Medium-Range Weather Forecasts Integrated Forecast System: 2. Data assimilation, J. Geophys. Res., 114, D13205, https://doi.org/10.1029/2008JD011115, 2009.

Cheng, Y., Dai, T., Goto, D., Schutgens, N. A. J., Shi, G., and Nakajima, T.: Investigating the

assimilation of CALIPSO global aerosol vertical observations using a four-dimensional

ensemble Kalman filter, Atmos. Chem. Phys, 19, 13445–13467, https://doi.org/10.5194/acp-

19-13445-2019, 2019.

Chen, D., Liu, Z., Ban, J., and Chen, M.: The 2015 and 2016 wintertime air pollution in China:

SO_2 emission changes derived from a WRF-Chem/EnKF coupled data assimilation system,

Atmos. Chem. Phys, 19, 8619–8650, https://doi.org/10.5194/acp-19-8619-2019, 2019a.

Chen, D., Liu, Z., Ban, J., Zhao, P., and Chen, M.: Retrospective analysis of 2015–2017

wintertime $PM_{2.5}$ in China: response to emission regulations and the role of meteorology, Atmos.

Chem. Phys., 19, 7409–7427, https://doi.org/10.5194/acp-19-7409-2019, 2019b.

Dai, T., Cheng, Y., Goto, D., Li, Y., Tang, X., Shi, G., and Nakajima, T.: Revealing the sulfur

dioxide emission reductions in China by assimilating surface observations in WRF-Chem,

Atmos. Chem. Phys., 21, 4357–4379, https://doi.org/10.5194/acp-21-4357-2021, 2021.

Dai, T., Cheng, Y., Suzuki, K., Goto, D., Kikuchi, M., Schutgens, N. A. J., Yoshida, M., Zhang,

P., Husi, L., Shi, G., and Nakajima, T.: Hourly Aerosol Assimilation of Himawari-8 AOT Using

the Four-Dimensional Local Ensemble Transform Kalman Filter, J. Adv. Model. Earth Syst.,

11, 680–711, https://doi.org/10.1029/2018MS001475, 2019.

Elbern, H., Strunk, A., Schmidt, H., and Talagrand, O.: Emission rate and chemical state

738   estimation by 4-dimensional variational inversion, Atmospheric Chemistry and Physics, 7(14),

739   3749–3769, https://doi.org/10.5194/acp-7-3749-2007, 2007.

740

741   Evensen, G.: Sequential data assimilation with a nonlinear quasi-geostrophic model using

742   Monte Carlo methods to forecast error statistics, Journal of Geophysical Research: Oceans, 99,

743   10143–10162, https://doi.org/10.1029/94JC00572, 1994.

744

745   Evensen, G.: The Ensemble Kalman Filter: theoretical formulation and practical

746   implementation, Ocean Dynam, 53, 343–367, https://doi.org/10.1007/s10236-003-0036-9,

747   2003.

748

749   Feng, S., Jiang, F., Jiang, Z., Wang, H., Cai, Z., and Zhang, L.: Impact of 3DVAR assimilation

750   of surface $PM_{2.5}$ observations on $PM_{2.5}$ forecasts over China during wintertime, Atmospheric

751   Environment, 187, 34-49, https://doi.org/10.1016/j.atmosenv.2018.05.049, 2018.

752

753   Feng, S., Jiang, F., Wang, H., Wang, H., Ju, W., Shen, Y., Zheng, Y., Wu, Z., and Ding,

754   A.: NOx emission changes over China during the COVID-19 epidemic inferred from surface

755   NO_2 observations, Geophysical   Research   Letters, 47,   e2020GL090080,

756   https://doi.org/10.1029/2020GL090080, 2020a.

757

758   Feng, S., Jiang, F., Wu, Z., Wang, H., Ju, W., and Wang, H.: CO emissions inferred from surface

759   CO observations over China in December 2013 and 2017, Journal of Geophysical Research:

760   Atmospheres, 125, https://doi.org/10.1029/2019JD031808, 2020b.

761

762 Feng, S., Jiang, F., Wu, Z., Wang, H., He, W., Shen, Y., Zhang, L., Zheng, Y., Lou, C., Jiang, Z.,

763 and Ju, W.: A Regional multi-Air Pollutant Assimilation System (RAPAS v1.0) for emission

764 estimates: system development and application, Geosci. Model Dev., 16, 5949–5977,

765 https://doi.org/10.5194/gmd-16-5949-2023, 2023.

766

767 Gao, M., Saide, P. E., Xin, J., Wang, Y., Liu, Z., Wang, Y., Wang, Z., Pagowski, M., Guttikunda,

768 S. K., and Carmichael, G. R.: Estimates of Health Impacts and Radiative Forcing in Winter

769 Haze in Eastern China through Constraints of Surface $PM_{2.5}$ Predictions, Environmental

770 Science & Technology, 51(4), 2178-2185, https://doi.org/10.1021/acs.est.6b03745, 2017.

771

772 Grell, G. A.: Prognostic Evaluation of Assumptions Used by Cumulus Parameterizations, Mon.

773 Wea. Rev., 121, 764–787, https://doi.org/10.1175/1520-

774 0493(1993)121<0764:PEOAUB>2.0.CO;2, 1993.

775

776 Grell, G., Peckham, S. E., Schmitz, R., McKeen, S. A., Frost, G., Skamarock, W. C., and Eder,

777 B.: Fully coupled "online" chemistry within the WRF model, Atmos. Environ, 39, 6957–6975,

778 https://doi.org/10.1016/j.atmosenv.2005.04.027, 2005.

779 Guenther, A., Hewitt, C. N., Erickson, D., Fall, R., Geron, C., Graedel, T., Harley, P., Klinger,

780 L., Lerdau, M., Mckay, W. A., Pierce, T., Scholes, B., Steinbrecher, R., Tallamraju, R., Taylor,

781 J., and Zimmerman, P.: A global model of natural volatile organic compound emissions, Journal

782 of Geophysical Research: Atmospheres, 100, 8873–8892, https://doi.org/10.1029/94JD02950,

783   1995.

785   Hong, S., Noh, Y., and Dudhia, J.: A new vertical diffusion package with an explicit treatment

786   of   entrainment   processes,   Mon.   Wea.   Rev,   134,   2318–2341,

787   https://doi.org/10.1175/MWR3199.1, 2006.

789   Huang, X.Y., Xiao, Q., Barker, D. M., Zhang, X., Michalakes, J., Huang, W., Henderson, T.,

790   Bray, J., Chen, Y., Ma, Z., Dudhia, J., Guo, Y., Zhang, X., Won, D., Lin, H., and Kuo, Y.: Four-

791   dimensional variational data assimilation for WRF: Formulation and preliminary results, Mon.

792   Weather Rev, 137, 299–314, https://doi.org/10.1175/2008MWR2577.1, 2009.

794   Hunt, B. R., Kalnay, E., Kostelich, E. J., Ott, E., Patil, D. J., Sauer, T., Szunyogh, I., Yorke, J.

795   A., and Zimin, A. V.: Four-dimensional ensemble Kalman filtering, Tellus A: Dynamic

796   Meteorology and Oceanography, 56(4), 273–277, https://doi.org/10.3402/tellusa.v56i4.14424,

797   2004.

799   Hunt, B. R., Kostelich, E. J., and Szunyogh, I.: Efficient data assimilation for spatiotemporal

800   chaos: a local ensemble transform Kalman filter, Physica D: Nonlinear Phenomena, 230, 112–

801   126, https://doi.org/10.1016/j.physd.2006.11.008, 2007.

803   Iacono, M. J., Delamere, J. S., Mlawer, E. J., Shephard, M. W., Clough, S. A., and Collins, W.

804   D.: Radiative forcing by long–lived greenhouse gases: Calculations with the AER radiative

805   transfer models, J. Geophys. Res., 113, D13103, https://doi.org/10.1029/2008JD009944, 2008.

806

807 Jin, J., Pang, M., Segers, A., Han, W., Fang, L., Li, B., Feng, H., Lin, H. X., and Liao, H.:

808 Inverse modeling of the 2021 spring super dust storms in East Asia, Atmos, Chem. Phys., 22,

809 6393–6410, https://doi.org/10.5194/acp-22-6393-2022, 2022.

810

811 Kong, L., Tang, X., Zhu, J., Wang, Z., Sun, Y., Fu, P., Gao, M., Wu, H., Lu, M., Wu, Q., Huang,

812 S., Sui, W., Li, J., Pan, X., Wu, L., Akimoto, H., and Carmichael, G. R.: Unbalanced emission

813 reductions of different species and sectors in China during COVID-19 lockdown derived by

814 multi-species surface observation assimilation, Atmos. Chem. Phys., 23, 6217–6240,

815 https://doi.org/10.5194/acp-23-6217-2023, 2023.

816

817 Kong, Y., Sheng, L., Li, Y., Zhang, W., Zhou, Y., Wang, W., and Zhao, Y.: Improving $PM_{2.5}$

818 forecast during haze episodes over China based on a coupled 4D-LETKF and WRF-Chem

819 system, Atmospheric Research, 249, 105366, https://doi.org/10.1016/j.atmosres.2020.105366,

820 2021.

821

822 Lorenc, A.C.: Analysis methods for numerical weather prediction, Q. J. R. Meteorol. Soc., 112,

823 1177–1194, https://doi.org/10.1002/qj.49711247414, 1986.

824

825 Luo, X., Tang, X., Wang, H., Kong, L., Wu, H., Wang, W., SONG, Y., Luo, H., Wang, Y., Zhu,

826 J., and Wang, Z.: Investigating the Changes in Air Pollutant Emissions over the Beijing-Tianjin-

827 Hebei Region in February from 2014 to 2019 through an Inverse Emission Method, Adv. Atmos.

Sci. 40, 601–618, https://doi.org/10.1007/s00376-022-2039-9, 2023.

Ma, C., Wang, T., Jiang, Z., Wu, H., Zhao, M., Zhuang, B., Li, S., Xie, M., Li, M., Liu, J., and Wu, R.: Importance of bias correction in data assimilation of multiple observations over eastern China using WRF-Chem/DART, Journal of Geophysical Research: Atmospheres, 125, e2019JD031465, https://doi.org/10.1029/2019JD031465, 2020.

Miyoshi, T., Yamane, S., and Enomoto, T.: Localizing the Error Covariance by Physical Distances within a Local Ensemble Transform Kalman Filter (LETKF), Scient. Online Lett. Atmos., 3, 89–92, https://doi.org/10.2151/sola.2007-023, 2007.

Morrison, H., Thompson, G., and Tatarskii, V.: Impact of Cloud Microphysics on the Development of Trailing Stratiform Precipitation in a Simulated Squall Line: Comparison of One– and Two–Moment Schemes, Mon. Wea. Rev., **137**, 991–1007, https://doi.org/10.1175/2008MWR2556.1, 2009.

Miyazaki, K., Eskes, H. J., and Sudo, K.: Global NOx emission estimates derived from an assimilation of OMI tropospheric NO_2 columns, Atmos. Chem. Phys., 12, 2263–2288, https://doi.org/10.5194/acp-12-2263-2012, 2012a.

Miyazaki, K., Eskes, H. J., Sudo, K., Takigawa, M., Weele, M. van., and Boersma, K. E.: Simultaneous assimilation of satellite NO_2, O_3, CO, and HNO_3 data for the analysis of

tropospheric chemical composition and emissions, Atmos. Chem. Phys., 12, 9545–9579, https://doi.org/10.5194/acp-12-9545-2012, 2012b.

Miyoshi, T.: LETKF source codes, GitHub, available at: https://github.com/takemasa-miyoshi/letkf, last access: 1 January 2024.

Ott, E., Hunt, B. R., Szunyogh, I., Zimin, A. V., Kostelich, E. J., Corazza, M., Kalnay, E., Patil, D. J., and Yorke, J. A.: A local ensemble Kalman filter for atmospheric data assimilation. Tellus A, 56, 415–428, https://doi.org/10.1111/j.1600-0870.2004.00076.x, 2004.

Pagowski, M., and Grell, G. A.: Experiments with the assimilation of fine aerosols using an ensemble Kalman filter, Journal of Geophysical Research, 117, D21302, https://doi.org/10.1029/2012JD018333, 2012.

Parrish, D. F. and Derber, J. C.: The National Meteorological Center's Spectral Statistical-Interpolation Analysis System, Mon. Weather Rev., 120, 1747–1763, https://doi.org/10.1175/1520-0493(1992)120<1747:TNMCSS>2.0.CO;2, 1992.

Peng, Z., Liu, Z., Chen, D., and Ban, J.: Improving $PM_{2.5}$ forecast over China by the joint adjustment of initial conditions and source emissions with an ensemble Kalman filter, Atmos. Chem. Phys., 17, 4837–4855, https://doi.org/10.5194/acp-17-4837-2017, 2017.

Peng, Z., Lei, L., Liu, Z., Sun, J., Ding, A., Ban, J., Chen, D., Kou, X., and Chu, K.: The impact of multi-species surface chemical observation assimilation on air quality forecasts in China,

874   Atmos. Chem. Phys., 18, 17387–17404, https://doi.org/10.5194/acp-18-17387-2018, 2018.

875

876   Rubin, J. I., Reid, J. S., Hansen, J. A., Anderson, J. L., Collins, N., Hoar, T. J., Hogan, T., Lynch,

877   P., McLay, J., Reynolds, C. A., Sessions, W. R., Westphal, D. L., and Zhang, J.: Development

878   of the Ensemble Navy Aerosol Analysis Prediction System (ENAAPS) and its application of

879   the Data Assimilation Research Testbed (DART) in support of aerosol forecasting, Atmos.

880   Chem. Phys., 16, 3927–3951, https://doi.org/10.5194/acp-16-3927-2016, 2016.

881

882   Schutgens, N. A. J., Miyoshi, T., Takemura, T., and Nakajima, T.: Sensitivity tests for an

883   ensemble Kalman filter for aerosol assimilation, Atmos. Chem. Phys., 10, 6583–6600,

884   https://doi.org/10.5194/acp-10-6583-2010, 2010.

885

886   Sekiyama, T. T., Tanaka, T. Y., Shimizu, A., and Miyoshi, T.: Data assimilation of CALIPSO

887   aerosol observations, Atmos. Chem. Phys., 10, 39–49, doi:10.5194/acp-10-39-2010, 2010.

888

889   Sun, W., Liu, Z., Chen, D., Zhao, P., and Chen, M.: Development and application of the

890   WRFDA-Chem three-dimensional variational (3DVAR) system: aiming to improve air quality

891   forecasting and diagnose model deficiencies, Atmos. Chem. Phys., 20, 9311–9329,

892   https://doi.org/10.5194/acp-20-9311-2020, 2020.

893

894   Schwartz, C. S., Liu, Z., Lin, H. C., and McKeen, S. A.: Simultaneous three-dimensional

895   variational assimilation of surface fine particulate matter and MODIS aerosol optical depth, J.

896   Geophys. Res., 117, D13202, https://doi.org/10.1029/2011JD017383, 2012.

897

898   Stockwell, W. R., Kirchner, F., Kuhn, M., and Seefeld, S.: A new mechanism for regional

899   atmospheric chemistry modeling, J. Geophys. Res., 102, 25847–25879,

900   https://doi.org/10.1029/97JD00849, 1997.

901

902   Tewari, M., Chen, F., Wang, W., Dudhia, J., LeMone, M. A., Mitchell, K., Ek, M., Gayno, G.,

903   Wegiel, J., and Cuenca, R. H.: Implementation and verification of the unified NOAH land

904   surface model in the WRF model, 20th conference on weather analysis and forecasting/16th

905   conference on numerical weather prediction, pp. 11–15, 2004.

906

907   van Donkelaar, A., Martin, R.V., Brauer, M., Hsu, N. C., Kahn, R. A., Levy, R. C., Lyapustin,

908   A., Sayer, A. M., and Winker, D. M.: Global estimates of fine particulate matter using a

909   combined geophysical-statistical method with information from satellites, models, and

910   monitors, Environ. Sci. Technol, 50, 3762–3772, https://doi.org/10.1021/acs.est.5b05833, 2016.

911

912   Wang, Z., Li, J., Wang, Z., Yang, W., Tang, X., Ge, B., Yan, P., Zhu, L., Chen, X., and Chen, H.:

913   Modeling study of regional severe hazes over mid-eastern China in January 2013 and its

914   implications on pollution prevention and control, Sci. China-Earth Sci., 57, 3–13,

915   https://doi.org/10.1007/s11430-013-4793-0, 2014.

916

917   Whitaker, J. S. and Hamill, T. M.: Ensemble data assimilation without perturbed observations,

Mon. Weather Rev., 130, 1913–1924, https://doi.org/10.1175/1520-0493(2002)130<1913:EDAWPO>2.0.CO;2, 2002.

Yan, S., Cao, H., Chen, Y., Wu, C., and Fan, H.: Spatial and temporal characteristics of air quality and air pollutants in 2013 in Beijing, Environ Sci Pollut Res., 23, 13996–14007, https://doi.org/10.1007/s11356-016-6518-3, 2016.

Yumimoto, K., and Takemura, T.: Direct radiative effect of aerosols estimated using ensemble-based data assimilation in a global aerosol climate model, Geophysical Research Letters, 38, L21802, https://doi.org/10.1029/2011GL049258, 2011.

Zheng, B., Cheng, J., Geng, G., Wang, X., Li, M., Shi, Q., Qi, J., Lei, Y., Zhang, Q., He, K.: Mapping anthropogenic emissions in China at 1 km spatial resolution and its application in air quality modeling, Science Bulletin, 66(6), 612-620, https://doi.org/10.1016/j.scib.2020.12.008, 2021.

Zhang, L., Li, Q., Wang, T., Ahmadov, R., Zhang, Q., Li, M., and Lv, M.: Combined impacts of nitrous acid and nitryl chloride on lower-tropospheric ozone: new module development in WRF-Chem and application to China, Atmos. Chem. Phys., 17, 9733–9750, https://doi.org/10.5194/acp-17-9733-2017, 2017.

Zhang, Q., Streets, D. G., Carmichael, G. R., He, K. B., Huo, H., Kannari, A., Klimont, Z., Park,

940   I. S., Reddy, S., Fu, J. S., Chen, D., Duan, L., Lei, Y., Wang, L. T., and Yao, Z. L.: Asian

941   emissions in 2006 for the NASA INTEX-B mission, Atmos. Chem. Phys., 9, 5131–5153,

942   https://doi.org/10.5194/acp-9-5131-2009, 2009.

943

944   Zhao, Y., Greybush, S. J., Wilson, R. J., Hoffman, R. N., and Kalnay, E.: Impact of assimilation

945   window length on diurnal features in a Mars atmospheric analysis, Tellus A, 67, 26042,

946   https://doi.org/10.3402/tellusa.v67.26042, 2015.

947

948   Zhang, Q., Ma, Q., Zhao, B., Liu, X., Wang, Y., Jia, B., and Zhang, X.: Winter haze over North

949   China Plain from 2009 to 2016: Influence of emission and meteorology, Environmental

950   Pollution, 242(B), 1308-1318, https://doi.org/10.1016/j.envpol.2018.08.019, 2018.

951

952   Zhan, D., Kwan, M., Zhang, W., Yu, X., Meng, B., and Liu, Q : The driving factors of air quality

953   index in China, Journal of Cleaner Production, 197, 1, 1342-1351,

954   https://doi.org/10.1016/j.jclepro.2018.06.108, 2018.